

Pre-perihelion Volatile Evolution of Interstellar Comet 3I/ATLAS Indicating Significant Contribution from Extended Source in the Coma

JUNCEN LI ,¹ XIAN SHI ,¹ MAN-TO HUI ,¹ AND JIANCHUN SHI ,¹

¹*Shanghai Astronomical Observatory, Chinese Academy of Sciences, 80 Nandan Road, 200030 Shanghai, People's Republic of China*

ABSTRACT

Interstellar comets provide rare opportunities for probing the diversity of refractory and volatile inventory around other stars. As the second ever interstellar comet, and the third interstellar object, 3I/ATLAS has been the focus of telescopic observations since its discovery in July 2025. Following the previous observations at multi-wavelengths, we present further radio observations of the 1665/1667 MHz ground-state OH lines and millimeter observations of the CO($J=1-0$) transition at 115.271 GHz that trace the coma H₂O and CO abundances, respectively. We derived OH production rates of $(1.32 \pm 0.47) \times 10^{28} \text{ s}^{-1}$ at 2.27 au and $(1.89 \pm 0.37) \times 10^{28} \text{ s}^{-1}$ at 1.96 au as well as an average CO production rate of $(5.75 \pm 1.91) \times 10^{27} \text{ s}^{-1}$ between 2.33 and 1.75 au, inferring a CO/H₂O ratio of $(28 \pm 11\%)$. With the mean HCN production rate of $2.5 \times 10^{25} \text{ s}^{-1}$ at 2.1 au reported by [N. X. Roth et al. \(2025a\)](#) and [I. M. Coulson et al. \(2025\)](#), we infer a CO/HCN ratio of (230 ± 76) . By synthesizing water production rates measured with instruments of different apertures, we found that the sublimation from extended source in the coma contributes significantly to 3I's pre-perihelion water measurements, accounting for up to 80% from 3 au to 2 au.

Keywords: Interstellar Objects (52); Small Solar System bodies (1469); Comets (280); Submillimeter astronomy / Submillimetre astronomy (1338)

1. INTRODUCTION

The discovery of interstellar objects (ISO) traversing the Solar System has opened a new window on the material inventory and planetesimal formation and evolution around other stars. While the first ISO 1I/‘Oumuamua showed no detectable coma and left its volatile composition ambiguous ([K. J. Meech et al. 2017](#)), the second 2I/Borisov displayed a “classical” cometary coma and tail ([D. Jewitt & J. Luu 2019](#)), enabling the first direct compositional measurements of an interstellar comet ([A. Fitzsimmons et al. 2019](#); [Z. Xing et al. 2020](#); [C. Opitom et al. 2021](#); [B. Yang et al. 2021](#)). Observations at different wavelengths of 2I revealed a suite of volatiles and radicals and, notably, relatively high CO abundances compared to many Solar System comets observed at similar heliocentric distances ([M. A. Cordiner et al. 2020](#); [D. Bodewits et al. 2020](#)). These measurements suggest that some interstellar comets may have formed in colder regions or experienced prolonged residence at very low temperatures, preserving CO-rich ices.

Email: jcli@shao.ac.cn, shi@shao.ac.cn

Discovered on July 1, 2025 by the Asteroid Terrestrial-impact Last Alert System (ATLAS), 3I/ATLAS (C/2025 N1, here after 3I) is the third confirmed ISO after 1I/‘Oumuamua and 2I/Borisov ([L. Denneau et al. 2025](#); [D. Z. Seligman et al. 2025](#)). Its discovery immediately attracted worldwide attention due to its unprecedented orbital properties, including an eccentricity exceeding 6 and a hyperbolic velocity over 50 km/s ([B. T. Bolin et al. 2025](#)). According to the Ōtautahi-Oxford model, 3I originated from the Milky Way’s thick disk, being the first one from that population entering our Solar System ([M. J. Hopkins et al. 2025](#)).

3I displayed the signs of a dust coma already at its discovery distance of 4.53 au ([M. R. Alarcon et al. 2025](#)), making it the second identified interstellar comet after 2I/Borisov. Extensive observations have been carried out since 3I’s discovery, spanning ultraviolet to infrared wavelengths, accumulating measurements of its developing activity. Clear signs of dust activity were detected by Hubble Space Telescope at 3.8 au, suggesting a mass loss rate of 6 to 60 kg/s ([D. Jewitt et al. 2025](#)). However, no detection of C₂, NH₂, CN, or [OI] were achieved at 3.46 au ([C. Opitom et al. 2025](#)). Furthermore, spectroscopic observations between 4.4 to 4.0 au

suggest 3I's dust particles have a relatively high ice fraction of $\sim 30\%$ (B. Yang et al. 2025) with a redder coma in optical spectrum than most Solar System comets (A. Alvarez-Candal et al. 2025; T. Karetta et al. 2025; C. Opitom et al. 2025), and a CO₂ dominated gas coma was detected by JWST and SPHEREx (M. A. Cordiner et al. 2025a; C. M. Lisse et al. 2025a). These studies show that 3I is markedly different from its predecessor 2I, or Solar System comets.

To understand the nature of 3I, the three primary species (H₂O, CO, and CO₂) content makes a key target of investigation as it helps determine its formation conditions and contributes to our understanding of molecular distribution in the original planetary system of this ISO. Among the three, ground-based monitoring of H₂O and CO vapour in 3I's coma is feasible. OH radicals, being the direct photodissociation products of H₂O molecules, serve as the primary tracer for water production rates in comets. The detections of OH in 3I's gas coma were performed at different wavelengths, with the first detection by the SWIFT space telescope at ultraviolet (Z. Xing et al. 2025) and follow-up at optical and radio wavelength (D. Hutsemékers et al. 2025; D. J. Pisano et al. 2025a,b; J. Crovisier et al. 2025). In this work, we report the results of pre-perihelion monitoring of 3I's CO and H₂O with the detections of CO(1-0) emission lines at 115 GHz and the earliest detection of OH at 1.6 GHz. Section 2 provides a description of the observations. Section 3 presents our results from these data. Section 4 discusses the evolution of H₂O production rate and the abundance of CO in 3I/ATLAS, and places this interstellar object into context with solar system comets measured to date.

2. OBSERVATIONS AND DATA REDUCTION

The 115 GHz measurements of CO were obtained from mid-August to September 2025 with the 13.7-m Millimeter-Wave Telescope in Delingha, China (see details in Z. Wang et al. 2020; J. Li et al. 2025a), for a total effective integration time of more than 10 hours. The HPBW (half power beam width) is $\sim 50''$, while the main beam efficiency η_B was $\sim 50\%$ at this frequency of 115 GHz. Observations of OH at 1.6 GHz were performed using the Tianma 65-m Radio Telescope (TMRT; see J. Li et al. 2025b) on 7 individual days in August and September, totaling above 10 hours of effective integration.

The pointing accuracy was verified daily using strong calibrator sources: IRC+10216 for the 115 GHz observations and W49N for the 1.6 GHz observations. Observation geometries of 3I were obtained using Horizons

Table 1. Characteristic of Target Spectral lines

Species	Transition	Frequency [GHz]
OH(² Π _{3/2})	<i>J</i> = 3/2, <i>F</i> = 1 – 1	1.665
	<i>J</i> = 3/2, <i>F</i> = 2 – 2	1.667
¹² CO	<i>J</i> = 1 – 0	115.271

System of Jet Propulsion Laboratory (JPL)² and the Minor Planet Ephemeris Service (MPEC)³. An observing log for all observations of 3I during these periods are shown in Table C1.

Data reduction and analysis were conducted with the CLASS package, part of the GILDAS software suite⁴. The processing included Doppler correction for the comet's radial velocity relative to the telescope during the observations (see Table C1). Considering the strong radio frequency interference in L band during our observations, spectral analysis was performed using only the right circular polarization data sometimes, as the left circular polarization data were significantly affected. A linear baseline was subtracted from each spectrum, excluding the region of the emission line. Individual spectra were then averaged using weights based on their rms noise levels.

3. RESULTS

To enhance the overall signal-to-noise ratio (S/N) given the limited daily integration time, spectra were averaged using weights derived from the noise level of each individual day. By integrating observations of Sep. 8 and 9, we first detected OH radical lines at 1667 MHz at pre-perihelion heliocentric distances (*r_h*) of around 2.27 au at above 3σ (Fig. 1). Subsequently, another detection of OH was obtained at around 1.96 au by integrating signals on Sep. 18 and 23. The CO(1-0) line was weaker at a level about 3σ by integrating several days of observations between Sep. 07 and Sep. 29 when 3I was traveling inbound from 2.33 to 1.75 au (Fig. 2).

3.1. OH lines analysis

The integrated intensity was computed over the velocity interval $[-1, 1] \text{ km} \cdot \text{s}^{-1}$ with its uncertainty esti-

² <https://ssd.jpl.nasa.gov/horizons/>

³ <https://minorplanetcenter.net/iau/MPEph/MPEph.html>

⁴ <http://www.iram.fr/IRAMFR/GILDAS>

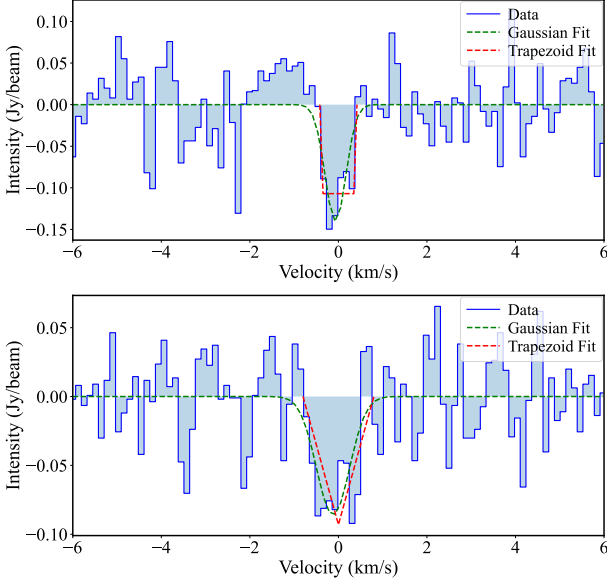


Figure 1. Averaged 18 cm OH lines (scaled to 1667 MHz) of 3I obtained in four observations with both a Gaussian and a trapezoid fit: Sep. 08 and 09 (top), Sep. 18 and 23 (bottom). Original observations are shown in Figure C2 and C3.

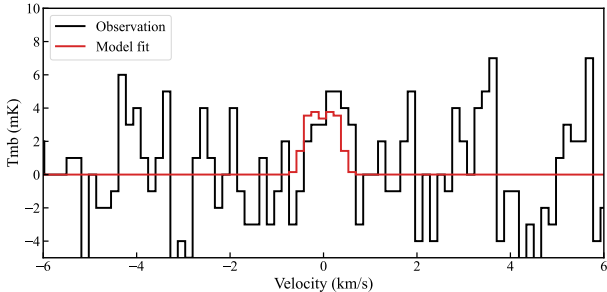


Figure 2. Averaged CO(1-0) line of 3I obtained from September observations. Original observations are shown in Figure C4.

mated from $\sqrt{n} \times \text{RMS} \times dv$, where dv is the channel width and n is the number of channels covering the line. Their values are summarized in Table 2.

The OH line profiles were analyzed using the symmetric standard trapezoid model for cometary radio observations (e.g., J. Crovisier et al. 2002; J. Li et al. 2025b). This model derives the OH velocity ($v_{\text{OH}} = v_p + v_e$) from the half-width of the trapezoid's lower base (Figure 1), where v_p is the parent molecule outflow velocity and v_e is the OH ejection velocity (D. Bockelée-Morvan et al. 1990). Gaussian-fitting of full width at half maximum (FWHM) offers an alternative velocity measure (N. Biver et al. 1999), which we applied to derive the Doppler shift relative to the cometary nucleus rest frame (Table 2).

The production rates of OH were derived from the integrated flux density, taking into consideration the quenching effect of OH (see detail in e.g. F. P. Schloerb & E. Gerard 1985; D. Bockelée-Morvan et al. 1990; M. N. Drozdovskaya et al. 2023; J. Li et al. 2025b). The population inversions of the Λ -doublet were primarily controlled by 3I's heliocentric velocity (v_h) due to Doppler-shifted solar UV excitation. All the parameters were listed in Table 2.

3.2. CO lines analysis

The production rate and expansion velocity of CO in 3I's were derived from the CO(1-0) spectrum. Using the density distribution based on the Haser model, we adopt a kinetic temperature (T_{kin}) of CO of 35 K (see Appendix A) and a production rate of water $Q_{\text{H}_2\text{O}} = 10^{28} \text{ s}^{-1}$ (see section 4.1). The level population of CO was computed by the non-LTE solver for cometary atmospheres from the Planetary Spectrum Generator (PSG, G. L. Villanueva et al. 2022). Collisions with H_2O molecules and electrons, and the radiative pumping by the solar radiation were take into account with an electron density scaling factor $x_{ne} = 0.2$ (M. A. Cordiner et al. 2025b; N. Biver et al. 2019; P. Hartogh et al. 2010). According to the escape probability method (D. Bockelée-Morvan 1987; V. Zakharov et al. 2007), we fitted the CO line profile, the expansion velocity and the production rate were derived (Table 3). The line profile showed a clear redward offset of the line center, similar to the HCN detection of ALMA in mid-September (N. X. Roth et al. 2025a).

4. DISCUSSION

4.1. Pre-perihelion Evolution of H_2O production rate

Figure 3 shows 3I's pre-perihelion H_2O production rate as a function of heliocentric distance measured with different facilities (A. Alvarez-Candal et al. 2025; D. Hutsemékers et al. 2025; M. A. Cordiner et al. 2025a; Z. Xing et al. 2025; C. M. Lisse et al. 2025b; J. Crovisier et al. 2025). Considering the divergence between different apertures, we separate the water measurements into two datasets. By fitting measurements obtained with large apertures ($\gtrsim 20000$ km, which covers the entire $\text{H}_2\text{O}/\text{OH}$ coma according to the radial surface brightness profiles from Z. Xing et al. 2025), we found a power-law relation of $Q_{\text{H}_2\text{O}} = (614.55 \pm 101.14) r_h^{(-5.91 \pm 0.23)} \times 10^{27} \text{ s}^{-1}$ (solid red line in Figure 3). In comparison, we also fit the VLT measurements with a much smaller aperture of 3000–4000 km (D. Hutsemékers et al. 2025) and derived a power-law relationship of $Q_{\text{H}_2\text{O}} = (825.95 \pm 747.57) r_h^{(-8.49 \pm 1.01)} \times 10^{27} \text{ s}^{-1}$ (solid blue line) in Figure 3. OH measurements were

Table 2. Spectral Characteristics of 3I/ALTAS

Species	$\langle r_h \rangle$	FWHM ^a	S^b	Doppler shift ^c	i^d	T_{bg}^e	v_{OH}^f	Q_{OH}^g
	[au]	[km · s ⁻¹]	[Jy · km · s ⁻¹]	[km · s ⁻¹]		[K]	[km · s ⁻¹]	[10 ²⁸ s ⁻¹]
OH	2.54	—	< 0.047	—	0.40	3.6	—	< 0.80
	2.27	0.553 ± 0.115	0.065 ± 0.023	-0.066	0.42	3.5	0.42 ± 0.04	1.32 ± 0.47
	1.96	0.877 ± 0.150	0.076 ± 0.015	-0.122	0.36	3.4	0.80 ± 0.08	1.89 ± 0.37

NOTE—^aThe FWHM line width obtained from a Gaussian fit; ^b The integrated intensity or 3σ upper limit; ^c The velocity offset of peak temperature; ^d Maser inversion from D. Despois et al. (1981); D. G. Schleicher & M. F. A'Hearn (1988); ^e The background temperature at 1667 MHz was measured by interpolating the continuum maps at 408 MHz (M. Remazeilles et al. 2015; C. G. T. Haslam et al. 1974) following the method mentioned in D. Despois et al. (1981); ^f The expansion velocity; ^g Production rate.

Table 3. Spectral Characteristics of 3I/ALTAS

Species	$\langle r_h \rangle$	FWHM	Doppler shift	T_{kin}	v_{exp}	Q_{CO}	$Q_{\text{CO}}/Q_{\text{H}_2\text{O}}$
	[au]	[km · s ⁻¹]	[km · s ⁻¹]	K	[km · s ⁻¹]	[10 ²⁷ s ⁻¹]	[%]
¹² CO	3.03-2.56	—	—	35	(0.30)	< 3.49	—
	2.33-1.75	0.643 ± 0.242	0.202	35	0.39 ± 0.14	5.75 ± 1.91	28 ± 11%
	3.03-1.75	0.537 ± 0.201	0.166	35	0.32 ± 0.12	4.05 ± 1.37	28 ± 15%

converted to H_2O by multiplying 1.1 (J. Crovisier 1989). In general, both slopes are consistent with the coma brightness slope and methanol evolution (from -5 to -8; N. X. Roth et al. 2025a; Q. Zhang & K. Battams 2025). As mentioned in the Q. Zhang & K. Battams (2025), the growth of brightness before ~ 2 au is much steeper than earlier trend (D. Jewitt et al. 2025), which may result from intensified H_2O sublimation after 3I crossed the H_2O snowline (Figure 3; also see Figure 2 in J. M. Trigo-Rodríguez et al. 2025).

4.2. An effective extended-source interpretation

The discrepancy between H_2O production rate measured with different sizes of apertures is obvious, as already discussed in several previous works on 3I's activity both pre-perihelion (M. A. Cordner et al. 2025a; Z. Xing et al. 2025; H. Tan et al. 2026) and post-perihelion (M. R. Combi et al. 2025). Moreover, water ice was detected in 3I's coma at an early stage beyond 4 au (B. Yang et al. 2025). These evidences point to possible contribution from water sublimation from icy particles in the coma. To quantify the contribution of extended source of water, we use an aperture-dependent two-component parameterization model of the production rate, and calculate the extended source fraction.

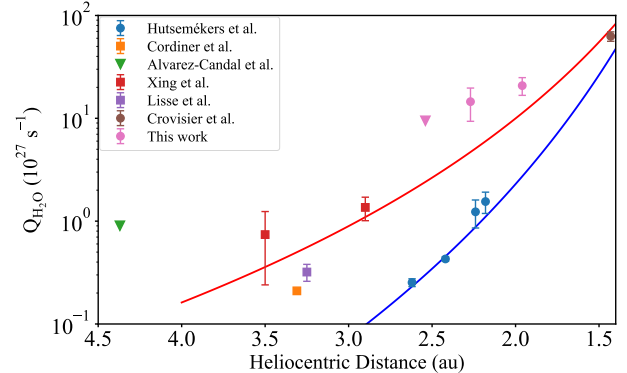


Figure 3. H_2O production rates of comet 3I as a function of heliocentric distance. The measurements from different sources are shown with different colors (A. Alvarez-Candal et al. 2025; D. Hutsemékers et al. 2025; M. A. Cordner et al. 2025a; Z. Xing et al. 2025; C. M. Lisse et al. 2025b; J. Crovisier et al. 2025). Error bars represent 1σ uncertainties. The symbol of circle, rectangle and triangle indicate the detection via OH, H_2O and upper limits, respectively. The red line shows the best-fit power-law curve with all data excluding those from VLT (D. Hutsemékers et al. 2025) and JWST (M. A. Cordner et al. 2025a). The blue one shows the best-fit power-law curve with VLT measurements only.

For a circular aperture of projected radius ρ (km), the effective production rate at heliocentric distance r_h is

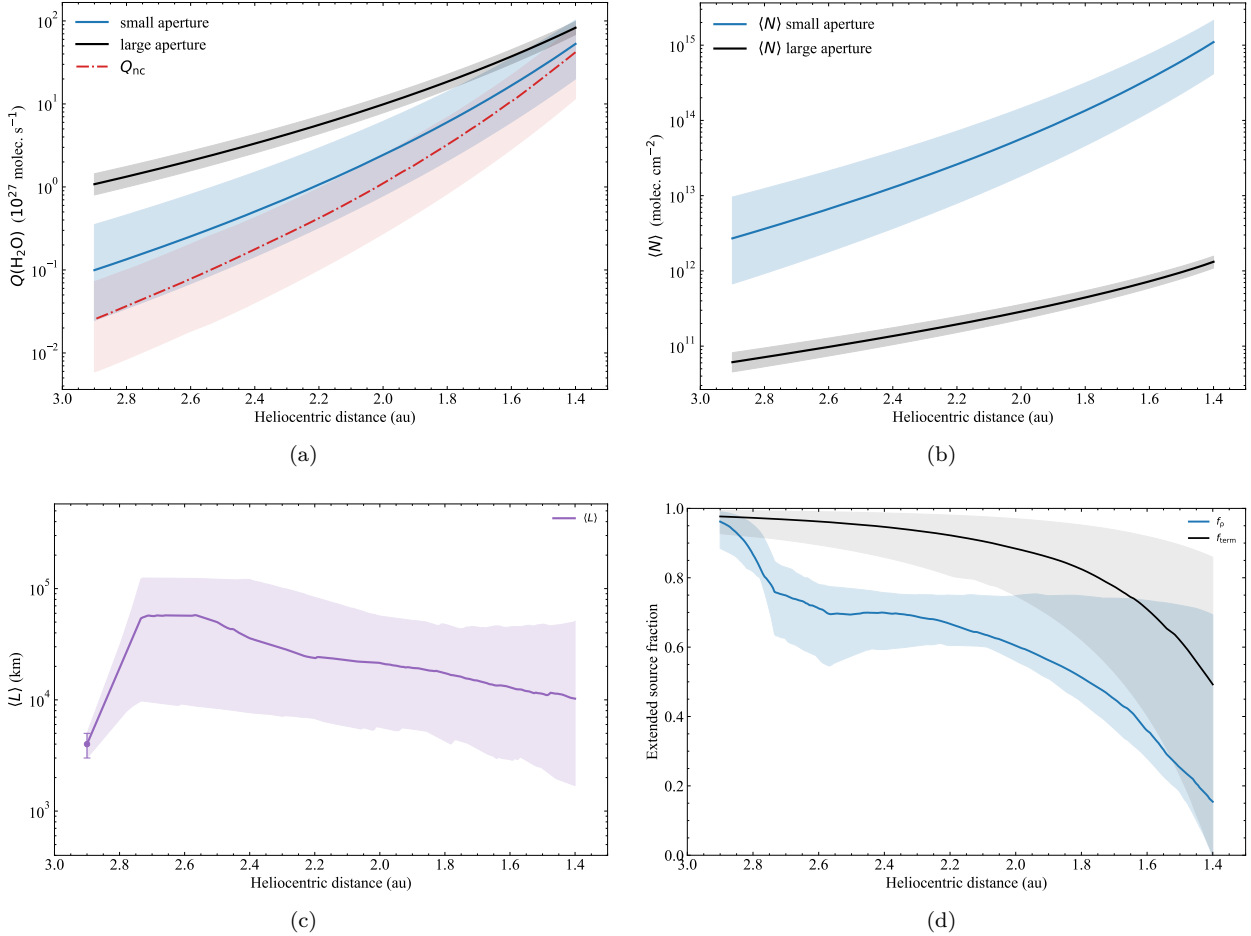


Figure 4. Contribution of extended source. (a) The power-law relationship between H₂O production rate and heliocentric distance. Black and blue solid lines are the fitted power-law relations with measurements done with large apertures ($\gtrsim 20000$ km) and small apertures (3000–4000 km), respectively. Red dashed line is the curve of production rate directly from the nucleus inferred from the model fitting. (b) Aperture-dependent column density calculated based on the production rate shown in (a). (c) Best-fitted equivalent scale-length of H₂O extended source with an initial of $L_{\text{ext}} = 4000^{+1000}_{-1000}$ km at 2.9 au is derived from Z. Xing et al. (2025). (d) Fraction of the extended source in the total water production within different apertures varying against heliocentric distances.

parameterized as:

$$Q_\rho = Q_{\text{nc}} + (Q_{\text{term}} - Q_{\text{nc}})[1 - \exp(-\rho/L_{\text{ext}})]. \quad (1)$$

We employed the term $L_{\text{ext}}(r_h)$ as the scale length of extended source at heliocentric distance r_h , defined as the nucleocentric distance where the contribution of extended source in aperture ρ reaches $(1 - 1/e)$ of its total contribution (the difference between the nuclear production rate Q_{nc} and the terminal production rate Q_{term}), and shows how rapidly the extended-source contribution saturates with increasing aperture. We consider the observations carried out with VLT/UVES representative of “small-aperture” measurements (D. Hutsemékers et al. 2025) which has an equivalent circle aperture ρ_{eq} is 1.93'' (Appendix B), corresponding to $\rho = [3360\text{--}3920]$ km at the distance of [2.4–2.7] au. Measurements reported by observations with facilities of large apertures,

namely Swift (aperture size scaled at $\rho = 10''$, Z. Xing et al. 2025), SPHEREx ($\rho = 12''$, C. M. Lisse et al. 2025b), Nançay ($\rho_{\text{eq}} = 3.77'$, J. Crovisier et al. 2025) and TMRT ($\rho = 5.8'$, this work), are considered to represent 3I’s total water production rate consisting both the nucleus emission and contribution from the extended source. We used a statistical model based on Monte-Carlo (MC) method to estimate the amount of H₂O produced via direct nucleus sublimation vs sublimation from icy grains in the extended coma (see details in Appendix B).

We found the best-fit H₂O production rate directly released from the nucleus to be $Q_{\text{nc}} = (1140^{+980}_{-783})r_h^{(10.30^{+0.20}_{-1.09})} \times 10^{27}$ s⁻¹ (Figure 4(a)). Figure 4(b) is a diagnostic conversion from the fitted/assumed $Q(\text{H}_2\text{O})$ curves to an average column density within

each aperture, using simplified parent-only Haser approximations (D. Bockelée-Morvan et al. 2004), and an expansion velocity of $0.85r_h^{-0.5}$ km·s $^{-1}$. For the fitting of L_{ext} , we used the radial brightness profile at 2.9 au observed by Swift (Z. Xing et al. 2025) as the starting point and treated L_{ext} as a free parameter. Figure 4(c) indicates L_{ext} experienced a brief period of increase at about 2.9 au to 2.6 au, which is consistent to the increase of radial surface brightness profiles from 3.5 au to 2.9 au in Z. Xing et al. (2025). Due to the increase of the temperature, L_{ext} subsequently decreases slowly when the comet approaches the Sun and the water ice sublimates more rapidly. We defined the fraction of extended-source in the entire coma

$$f_{\text{term}} = \frac{Q_{\text{term}} - Q_{\text{nc}}}{Q_{\text{term}}} \quad (2)$$

and in aperture ρ

$$f_{\rho} = \frac{Q_{\rho} - Q_{\text{nc}}}{Q_{\rho}}. \quad (3)$$

Figure 4(d) shows $f_{\text{term}} \sim 0.5$ near 1.4 au and ~ 0.9 at 2.9 au implying that a large fraction of the “large-aperture” production is attributed to the extended source. Note that the fraction may be overestimated outside the 2.6 au as the “small-aperture” measurements were all obtained within 2.6 au. The wide gray band at the large aperture demonstrate that with measurements at two apertures, Q_{nc} and L_{ext} are not sufficient to be confined within a narrow margin of error among MC realizations. Therefore, the existence of a strong extended contribution is robust, but its exact fraction is only loosely constrained.

The significant contribution of sublimation of extended source in the coma of 3I beyond 2 au from the Sun is similar to what was found with the long-period comet C/2009 P1 (Garradd), whose extended-source (icy grains/chunks) persists at distances beyond 10^6 km from the nucleus and contributes more than 60% of the water production rate at $r_h \sim 2$ au (M. R. Combi et al. 2013). For other comets with confirmed extended-source sublimation in the coma, their derived ratios also vary across different methods (e.g., 103P at around its perihelion, 25-40% in L. M. Feaga & J. M. Sunshine 2025, 85% in Y. Shou et al. 2025, 77% in N. Fougere et al. 2013), and more depending on the observation data used at different r_h (e.g., 46P, N. X. Roth et al. 2021; M. M. Knight et al. 2021; S. Protopapa et al. 2021; B. P. Bonev et al. 2021; T. Karetta et al. 2023). Meanwhile, the factors related to the occurrence of extended sources and their contributions remain difficult to constrain. In most cases, extended sublimation is associated with the activity of highly volatile species, such as

CO₂ in C/2013 US10 (S. Protopapa et al. 2018), 103P (S. Protopapa et al. 2014), CO in C/2009 P1 (L. M. Feaga et al. 2014), where these volatiles could eject dust particles with high water ice content, especially at larger heliocentric distances. Given the relatively high amount of carbon dioxide measured around 3I (M. A. Cordiner et al. 2025a; C. M. Lisse et al. 2025b), it is possible that such mechanism is at work for 3I’s secondary sublimation. Further confirmation will require high-resolution observations or space missions.

4.3. CO abundance

3I exhibited a CO₂-dominated coma with relative low CO and H₂O occupied in coma during the early stage of its activity beyond 3 au, which results in the very different CO/H₂O ratio about 31% and 166% in two works, respectively (C. M. Lisse et al. 2025b; M. A. Cordiner et al. 2025a). Using CO and H₂O production rates retrieved by radio observations, we derived a CO/H₂O ratio of $(28 \pm 11)\%$, which place 3I well above the typical Solar System cometary CO abundance of $\sim 4\%$ (L. Paganini et al. 2014; N. Biver et al. 2024a). The value is similar to some “CO-rich” Oort Cloud comets at about 2 au like C/2012 X1 (LINEAR) of $(32 \pm 5)\%$, C/2009 P1 (Garradd) of $(19 \pm 2)\%$, C/2008 Q3 (Garradd) of $(26 \pm 4)\%$ (N. Biver et al. 2012, 2014; M. A. Cordiner et al. 2020; O. Harrington Pinto et al. 2022), whereas the interstellar comet 2I/Borisov reaches above 60% (M. A. Cordiner et al. 2020; D. Bodewits et al. 2020) (Figure 5). Within uncertainties, 3I’s CO/H₂O ratio is intermediate between the upper envelope of Solar System comets and the elevated CO abundance reported for 2I/Borisov, suggesting a comparatively CO-enriched volatile inventory relative to canonical Solar System comet compositions. But H₂O production rate increased more rapidly than CO when 3I got close to the Sun, leading the CO/H₂O ratio decreasing to the level of Oort Cloud comets (Figure 5).

Comet 3I has an estimated CO/HCN about 230 ± 76 under an assumption of $Q_{\text{HCN}} = 2.5 \times 10^{25} \text{ s}^{-1}$ (N. X. Roth et al. 2025a; I. M. Coulson et al. 2025), which is higher than the CO/HCN values reported for most Solar System comets at around 2 au (see Figure 4 in M. A. Cordiner et al. 2020), but remains below the unusually large ratio inferred for the interstellar comet 2I/Borisov (630^{+200}_{-340}) (M. A. Cordiner et al. 2020). While 2I/Borisov’s CO/HCN is described as exceeding that of any previously observed comet except the extreme case of C/2016 R2 (PANSTARRS) (CO/HCN=26,400 at $r_h=2.8$ au, N. Biver et al. 2018), 3I’s intermediate value nonetheless also indicates a comparatively CO-enriched composition relative to HCN

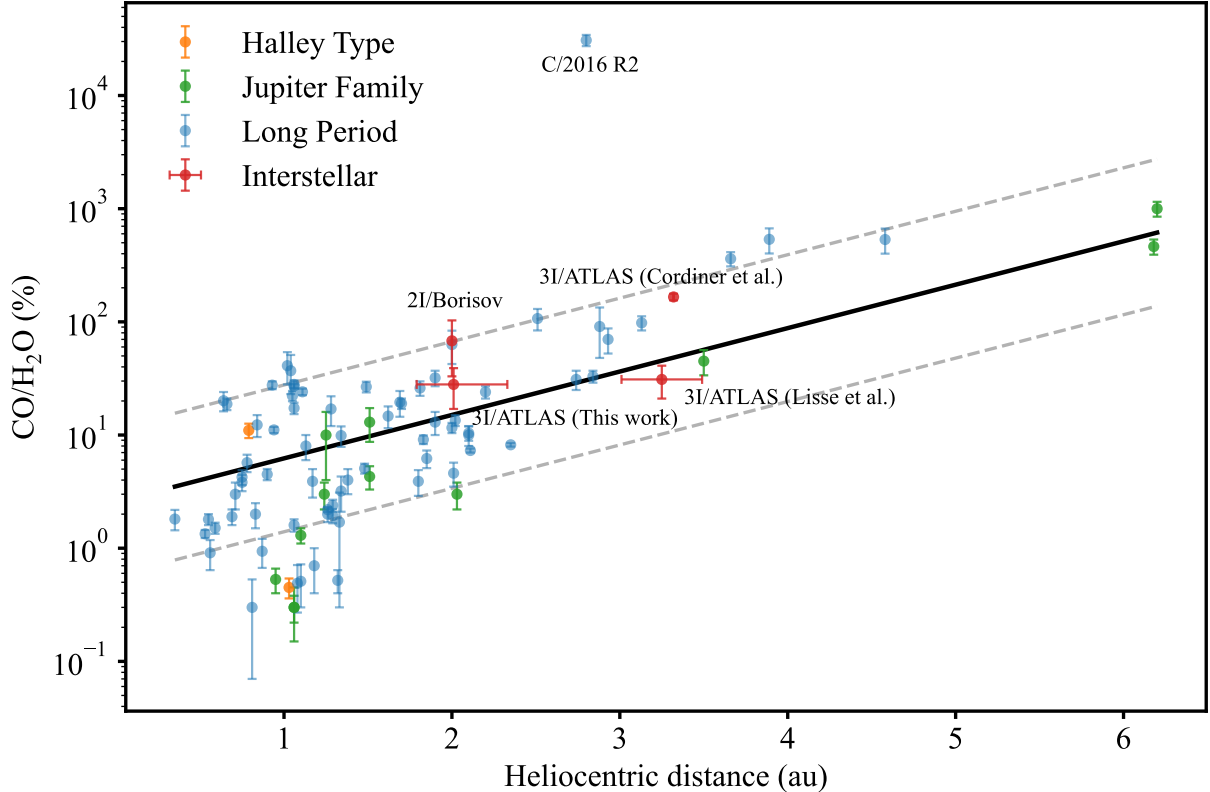


Figure 5. Coma CO/H₂O mixing ratios as a function of heliocentric distance for Solar System comets and interstellar comets. The measurements of different dynamic group are shown with different colors. All data are summarized from the collections in previous works (N. Dello Russo et al. 2016; A. J. McKay et al. 2019; O. Harrington Pinto et al. 2022) and recent observations (N. Biver et al. 2018, 2024b; D. Bockelée-Morvan et al. 2022; N. Dello Russo et al. 2022; N. X. Roth et al. 2025b; M. A. Cordiner et al. 2020; C. E. Woodward et al. 2025). A log-linear curve is fitted to the Solar System comets, with 1σ prediction band shown as dashed gray lines. The other two results of 3I/ATLAS are from M. A. Cordiner et al. (2025a) and C. M. Lisse et al. (2025b).

but more similar to Solar System cometary abundances than 2I.

5. CONCLUSIONS

We conducted radio observations of 3I in August and September, 2025, focusing on the monitoring of OH as a proxy for H₂O and on the detection of CO together with its isotopologues.

From the 18-cm OH maser lines observed with TMRT, we derived OH production rates for two epochs: $(1.32 \pm 0.47) \times 10^{28} \text{ s}^{-1}$ at 2.27 au and $(1.89 \pm 0.37) \times 10^{28} \text{ s}^{-1}$ at 1.96 au, adopting an expansion velocity of $\sim 0.4\text{--}0.8 \text{ km s}^{-1}$ for September. Combined with results from previous work, we obtained a pre-perihelion heliocentric-distance dependence for H₂O production with a power-law index of $\sim 5\text{--}6$, while noting that the rapid rise in water sublimation inside the ~ 2.7 au snow line should be taken into account. Overall, we find that the H₂O production rate increases more rapidly inside the snow line, consistent in brightness with the expected behavior, although the evolution between ~ 2 and 3 au before

perihelion remains complex and requires additional measurements. We note that, MeerKAT obtained near perihelion OH production rate measurements with about $2'$ beam size could provide further constraints on production rate and extended-source fraction (D. J. Pisano et al. 2025a,b).

Using the CO($J=1\text{--}0$) line, we derived production rates of $(5.75 \pm 1.91 \times 10^{27} \text{ s}^{-1})$ at around 2.01 au. The CO production rate increased as 3I moved closer to the Sun, but more slowly than H₂O. Based on these measurements, we estimate CO/H₂O = $(28 \pm 11)\%$ at ~ 2.01 au. This value is lower than the last interstellar comet 2I, but still higher compared to the mean value of Solar System comets.

Based on the H₂O production rates obtained from different apertures, we estimated the fraction of extended sources in the coma of 3I during its pre-perihelion passage. The extended-source fraction accounted for approximately over 80% around 2–3 au, then decreased to about 50% at perihelion.

ACKNOWLEDGMENTS

The authors thank all the staff of the Tianma-65m Radio Telescope at Shanghai Astronomical Observatory and the 13.7-m Millimeter Wave Telescope at Purple Mountain Observatory for their assistance. This work is financially supported by the National Natural Science Foundation of China (No. 12233003).

Facilities: PMO: 13.7m, SHAO: TMRT

Software: GILDAS and CLASS (J. Pety 2018), astropy (Astropy Collaboration et al. 2013, 2018, 2022), Planetary Spectrum Generator (PSG; G. L. Villanueva et al. 2022), Matplotlib (J. D. Hunter 2007), Numpy (C. R. Harris et al. 2020).

APPENDIX

A. SPECTRAL MODELING

A.1. Spectral fitting

We modeled the observed spectrum by using a spherically symmetric coma (L. Haser et al. 2020; L. Haser 1957) and fitting for two global parameters: the expansion velocity v_{exp} and the production rate Q . The non-LTE excitation calculation provides the radial fractional populations at high and low level (n_u and n_l). For each trial (v_{exp}, Q), we compute a beam-averaged main-beam brightness temperature spectrum $T_{\text{mb}}(v)$ by integrating the line emissivity along the line of sight and convolving with a 2D Gaussian telescope beam. Optical-depth effects are accounted for using an escape-probability factor $\beta(\tau)$ in an LVG/Sobolev approximation (G. B. Rybicki 1984, see details in N. Biver 1997 and D. Bockelee-Morvan 1987). The microscopic line profile is taken as a Gaussian, while the bulk outflow is mapped into the spectrum through the projected line-of-sight velocity field. The model spectrum is computed by integrating the emissivity along the line of sight and averaging over a 2D Gaussian telescope beam. The final beam-averaged specific intensity is normalized by the numerical beam integral. The fit is performed over a defined velocity window around line center, while the final best-fitting model is evaluated and plotted over the full velocity range for presentation. Parameter uncertainties are estimated from Monte-Carlo resampling of the spectrum using the measured channel RMS. We report conservative 1σ errors based on these estimates.

A.2. Assumption of Kinetic Temperature

In considering the kinetic temperature of the coma, we adopted a range of 20–50 K, consistent with values used in M. A. Cordiner et al. (2020) and I. M. Coulson et al. (2025) at approximately 2 au. This range is also supported by the radial temperature profile derived from CH₃OH lines on September 22 at large nucleocentric distances. In the case of $x_{\text{ne}} = 0.2$, the derived CO production rates were $(4.60 \pm 1.58) \times 10^{27} \text{ s}^{-1}$ at 20 K and $(6.81 \pm 2.24) \times 10^{27} \text{ s}^{-1}$ at 50 K. Since the choice of kinetic temperature within this range does not significantly affect the production rate, we adopted a mean value of 35 K for further analysis in the main text.

B. WATER PRODUCTION RATE WITH EXTENDED SOURCE

We model the aperture dependence of the retrieved H₂O production rate with a two-component prescription: a nucleus source plus a extended source (inferred from the relationship between column density and nucleocentric distance used in S. Protopapa et al. (2014), similar to the trend in L. M. Feaga & J. M. Sunshine 2025 and the Q-curve in X. Xie & M. J. Mumma 1996; N. Dello Russo et al. 1998; M. A. DiSanti et al. 2001, 2016; B. P. Bonev et al. 2006, 2017, 2021; G. L. Villanueva et al. 2011).

To compare production rates measured with apertures of different shapes, we convert a rectangular spectroscopic slit to an equivalent circular aperture ρ_{eq} . In the isotropic, constant-velocity outflow approximation, the column density scales as $N \propto \frac{1}{\rho}$ where ρ is the projected nucleocentric distance. The quantity that enters the aperture-averaged measurement is therefore $I = \int_A \frac{1}{\rho} \text{da}$, so that $\rho_{\text{eq}} = \frac{1}{2\pi} \int_A \frac{1}{\rho} \text{da}$. If the slit is a rectangle of length L and width W (e.g., VLT, J. Manfroid et al. 2021), centered on the nucleus, with $a = L/2$, $b = W/2$ and $r = \sqrt{a^2 + b^2}$, then

$$\rho_{\text{eq}} = \frac{2}{\pi} \left[a \ln\left(\frac{b+r}{a}\right) + b \ln\left(\frac{a+r}{b}\right) \right]. \quad (\text{B1})$$

We propagated the uncertainties of the empirical aperture-dependent production-rate laws as stated in Equation 1 using a Monte Carlo (MC) resampling scheme (J. C. for Guides in Metrology 2008; R. Andrae 2010). Each aperture

is described by a power law $Q_{\text{nc}} = Q_{n_0} r_h^{-n}$ (units: 10^{27} s^{-1}), where Q_{n_0} is the production rate at $r_h = 1 \text{ au}$, n is the power-law index, they are taken with their quoted 1σ uncertainties. In the MC, we draw n_n from a normal distribution $n \sim N(n_0, \sigma_n)$. We draw Q_{n_0} from $Q_{n_0} \sim N(Q_0, \sigma_Q)$ and enforce $Q_{n_0} > 0$ via simple rejection (a few resampling attempts) followed by clipping at zero. We assume Q_{n_0} and n are independent and do not include covariance between parameters or between the two apertures. For each MC realization we compute the corresponding curves $Q_{\text{small}}(r_h)$ and $Q_{\text{large}}(r_h)$. At each r_h , we summarize the ensemble by the median (50%) as the central estimate and the 16%-84% percentile interval as an uncertainty band 1σ , which corresponds to the central 68% interval of the MC distribution. To propagate these observational uncertainties into the secondary-sublimation (extended source) inversion, we perform MC refits in production-space. For each selected MC realization, we treat the large-aperture curve as the coma-integrated production rate, $Q_{\text{term}}(r_h) \simeq Q_{\text{large}}(r_h)$. We convert the angular aperture radius to a projected physical radius and fit the global model parameters (Q_{n_0} , n , L_{ext}) in a global heliocentric dependence $Q_{\text{nc}} = Q_{n_0} r_h^{-n}$ and L_{ext} as a free parameter at each heliocentric distance. Each refit yields the derived curves $Q_{\text{nc}}(r_h)$, $L_{\text{ext}}(r_h)$ as well as the fraction of extended-source in total production rate f_{term} (Equation 2) and in aperture-dependent production rate (Equation 3). We report MC medians and 1σ bands for all fitted parameters and derived quantities. In Figure 4, the displayed “best” curves correspond to the MC median solution for consistency with the MC uncertainty envelopes. This MC procedure captures the uncertainty propagated from the empirical power-law fits, while uncertainties in aperture and additional systematic effects (e.g., instrument-to-instrument differences, model-form uncertainty, or parameter correlations) are not included and should be interpreted as potential additional sources of error.

This analysis intentionally treats the $Q(r_h)$ curves as given and does not attempt to homogenize instrumental or excitation/fluorescence differences among different wavelengths. Consequently, the inferred parameters (especially L_{ext}) should be interpreted as effective quantities that encode both physical coma extension and any systematic differences inherent to the literature derivations. In fact, the reasonable prior on L_{ext} has little effect on the total extended-source fraction (< 5%), as we assumed a wide range of [3000-5000] km at 2.9 au. Despite these limitations, the combined small-aperture vs coma-covering constraints provide a practical quantification of the scale dependence and the degree to which an extended source is required to reconcile the reported activity levels.

C. OBSERVING LOG AND SPECTRUM

D. H_2O AND CO PRODUCTION RATES

REFERENCES

Alarcon, M. R., Serra-Ricart, M., Licandro, J., et al. 2025, The Astronomer’s Telegram, 17264, 1

Alvarez-Candal, A., Rizos, J. L., Lara, L. M., et al. 2025, A&A, 700, L10, doi: [10.1051/0004-6361/202556338](https://doi.org/10.1051/0004-6361/202556338)

Andrae, R. 2010, arXiv e-prints, arXiv:1009.2755, doi: [10.48550/arXiv.1009.2755](https://doi.org/10.48550/arXiv.1009.2755)

Astropy Collaboration, Robitaille, T. P., Tollerud, E. J., et al. 2013, A&A, 558, A33, doi: [10.1051/0004-6361/201322068](https://doi.org/10.1051/0004-6361/201322068)

Astropy Collaboration, Price-Whelan, A. M., Sipőcz, B. M., et al. 2018, AJ, 156, 123, doi: [10.3847/1538-3881/aabc4f](https://doi.org/10.3847/1538-3881/aabc4f)

Astropy Collaboration, Price-Whelan, A. M., Lim, P. L., et al. 2022, ApJ, 935, 167, doi: [10.3847/1538-4357/ac7c74](https://doi.org/10.3847/1538-4357/ac7c74)

Biver, N. 1997, PhD thesis, -

Biver, N., Dello Russo, N., Opitom, C., & Rubin, M. 2024a, in Comets III, ed. K. J. Meech, M. R. Combi, D. Bockelée-Morvan, S. N. Raymond, & M. E. Zolensky, 459–498, doi: [10.2458/azu_uapress_9780816553631-ch015](https://doi.org/10.2458/azu_uapress_9780816553631-ch015)

Biver, N., Bockelée-Morvan, D., Crovisier, J., et al. 1999, AJ, 118, 1850, doi: [10.1086/301033](https://doi.org/10.1086/301033)

Biver, N., Bockelée-Morvan, D., Lis, D. C., et al. 2012, in LPI Contributions, Vol. 1667, Asteroids, Comets, Meteors 2012, ed. LPI Editorial Board, 6330

Biver, N., Agundez, M., Milam, S., et al. 2014, in Asteroids, Comets, Meteors 2014, 46

Biver, N., Bockelée-Morvan, D., Paubert, G., et al. 2018, A&A, 619, A127, doi: [10.1051/0004-6361/201833449](https://doi.org/10.1051/0004-6361/201833449)

Biver, N., Bockelée-Morvan, D., Hofstadter, M., et al. 2019, A&A, 630, A19, doi: [10.1051/0004-6361/201834960](https://doi.org/10.1051/0004-6361/201834960)

Biver, N., Bockelée-Morvan, D., Handzlik, B., et al. 2024b, A&A, 690, A271, doi: [10.1051/0004-6361/202450921](https://doi.org/10.1051/0004-6361/202450921)

Bockelée-Morvan, D. 1987, A&A, 181, 169

Bockelée-Morvan, D., Crovisier, J., & Gérard, E. 1990, A&A, 238, 382

Bockelée-Morvan, D., Crovisier, J., Mumma, M. J., & Weaver, H. A. 2004, in Comets II, ed. M. C. Festou, H. U. Keller, & H. A. Weaver, 391

Table C1. Observation Log of 3I/ATLAS

Date (2025)	UT Time	$\langle r_h \rangle^a$	$\langle \Delta \rangle^b$	$\langle \alpha \rangle^c$	$\langle \psi \rangle^d$	$\langle v_r \rangle^e$
		[au]	[au]	[$^{\circ}$]	[$^{\circ}$]	[$\text{km} \cdot \text{s}^{-1}$]
18-cm OH lines						
Aug. 26	08:54-13:00	2.68	2.60	22.0	83.9	-7.05
Sep. 01	05:54-12:00	2.50	2.57	22.9	74.7	-5.20
Sep. 03	05:42-12:00	2.44	2.57	23.0	71.5	-4.69
Sep. 08	05:48-11:42	2.30	2.56	23.2	63.9	-3.70
Sep. 09	05:48-11:42	2.27	2.55	23.2	62.3	-3.81
Sep. 18	05:00-10:42	2.02	2.54	22.0	48.8	-3.68
Sep. 23	03:42-09:42	1.89	2.52	20.6	41.4	-4.40
$^{12}\text{CO}(J = 1 - 0)$ lines						
Aug. 15	10:25-12:59	3.03	2.66	19.1	101.6	-13.04
Aug. 16	10:06-12:57	3.00	2.65	19.4	99.8	-12.41
Aug. 18	09:51-11:37	2.93	2.64	20.0	96.7	-11.27
Aug. 24	09:23-12:27	2.75	2.60	21.6	87.1	-8.09
Aug. 30	08:09-10:26	2.56	2.58	22.6	77.8	-5.92
Sep. 07	08:02-09:19	2.33	2.56	23.2	65.4	-4.13
Sep. 11	07:43-09:04	2.21	2.55	23.0	59.3	-3.77
Sep. 13	06:56-09:11	2.16	2.55	22.8	56.3	-3.68
Sep. 15	06:52-08:49	2.10	2.54	22.6	53.3	-3.70
Sep. 17	06:17-08:43	2.05	2.54	22.2	50.3	-3.81
Sep. 23	06:03-08:16	1.89	2.52	20.6	41.4	-4.51
Sep. 25	06:16-08:40	1.84	2.52	19.8	38.5	-4.85
Sep. 27	05:50-08:06	1.79	2.51	18.9	35.5	-5.33
Sep. 29	05:26-07:45	1.75	2.51	18.0	32.6	-5.85

NOTE—^aMean heliocentric distance during observation time; ^bMean geocentric distance; ^cMean solar phase angle (Sun-object-Earth); ^dMean solar elongation angle (Sun-Earth-object); ^eMean radial velocity.

Bockelée-Morvan, D., Biver, N., Schambeau, C. A., et al. 2022, *A&A*, 664, A95, doi: [10.1051/0004-6361/202243241](https://doi.org/10.1051/0004-6361/202243241)

Bodewits, D., Noonan, J. W., Feldman, P. D., et al. 2020, *Nature Astronomy*, 4, 867, doi: [10.1038/s41550-020-1095-2](https://doi.org/10.1038/s41550-020-1095-2)

Bolin, B. T., Belyakov, M., Fremling, C., et al. 2025, *MNRAS*, 542, L139, doi: [10.1093/mnrasl/slaf078](https://doi.org/10.1093/mnrasl/slaf078)

Bonev, B. P., Mumma, M. J., DiSanti, M. A., et al. 2006, *ApJ*, 653, 774, doi: [10.1086/508452](https://doi.org/10.1086/508452)

Bonev, B. P., Villanueva, G. L., DiSanti, M. A., et al. 2017, *AJ*, 153, 241, doi: [10.3847/1538-3881/aa64dd](https://doi.org/10.3847/1538-3881/aa64dd)

Bonev, B. P., Dello Russo, N., DiSanti, M. A., et al. 2021, *PSJ*, 2, 45, doi: [10.3847/PSJ/abd03c](https://doi.org/10.3847/PSJ/abd03c)

Combi, M. R., Mäkinen, J. T. T., Bertaux, J.-L., et al. 2013, *Icarus*, 225, 740, doi: [10.1016/j.icarus.2013.04.030](https://doi.org/10.1016/j.icarus.2013.04.030)

Combi, M. R., Mäkinen, T., Bertaux, J.-L., et al. 2025, *arXiv e-prints*, arXiv:2512.22354, doi: [10.48550/arXiv.2512.22354](https://doi.org/10.48550/arXiv.2512.22354)

Cordiner, M. A., Milam, S. N., Biver, N., et al. 2020, *Nature Astronomy*, 4, 861, doi: [10.1038/s41550-020-1087-2](https://doi.org/10.1038/s41550-020-1087-2)

Cordiner, M. A., Roth, N. X., Kelley, M. S. P., et al. 2025a, *ApJL*, 991, L43, doi: [10.3847/2041-8213/ae0647](https://doi.org/10.3847/2041-8213/ae0647)

Cordiner, M. A., Gibb, E. L., Kisiel, Z., et al. 2025b, *Nature Astronomy*, 9, 1476, doi: [10.1038/s41550-025-02614-7](https://doi.org/10.1038/s41550-025-02614-7)

Coulson, I. M., Kuan, Y.-J., Charnley, S. B., et al. 2025, *arXiv e-prints*, arXiv:2510.02817, doi: [10.48550/arXiv.2510.02817](https://doi.org/10.48550/arXiv.2510.02817)

Crovisier, J. 1989, *A&A*, 213, 459

Crovisier, J., Biver, N., & Bockelée-Morvan, D. 2025, *Central Bureau Electronic Telegrams*, 5625, 1

Crovisier, J., Colom, P., Gérard, E., Bockelée-Morvan, D., & Bourgois, G. 2002, *A&A*, 393, 1053, doi: [10.1051/0004-6361:20020673](https://doi.org/10.1051/0004-6361:20020673)

Dello Russo, N., DiSanti, M. A., Mumma, M. J., Magee-Sauer, K., & Rettig, T. W. 1998, *Icarus*, 135, 377, doi: [10.1006/icar.1998.5990](https://doi.org/10.1006/icar.1998.5990)

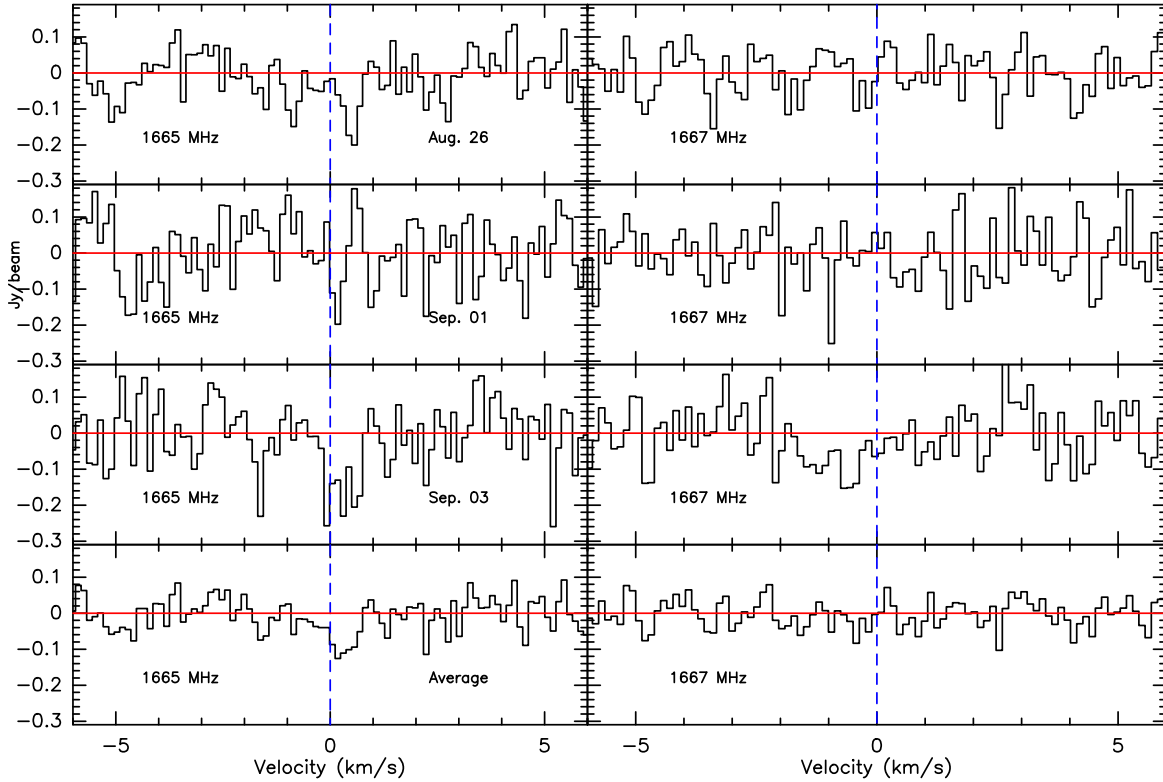


Figure C1. Averaged 18 cm OH lines of 3I/ATLAS observed on three separate days: August 26 (top), September 1 (upper middle), September 3 (lower middle), 2025, weighted averages of the 1667 and 1665 MHz lines (bottom). 1665 and 1667 MHz lines are shown in left and right, respectively. The vertical scale is scaled to the flux intensity, and the horizontal scale is the Doppler velocity in the comet rest frame. The velocity resolution is $0.1288 \text{ km} \cdot \text{s}^{-1}$ after smooth.

Dello Russo, N., Kawakita, H., Vervack, R. J., & Weaver, H. A. 2016, *Icarus*, 278, 301, doi: [10.1016/j.icarus.2016.05.039](https://doi.org/10.1016/j.icarus.2016.05.039)

Dello Russo, N., Vervack, R. J., Kawakita, H., et al. 2022, *PSJ*, 3, 6, doi: [10.3847/PSJ/ac323c](https://doi.org/10.3847/PSJ/ac323c)

Denneau, L., Siverd, R., Tonry, J., et al. 2025, Minor Planet Electronic Circulars, 2025-N12, doi: [10.48377/MPEC/2025-N12](https://doi.org/10.48377/MPEC/2025-N12)

Despois, D., Gerard, E., Crovisier, J., & Kazes, I. 1981, *A&A*, 99, 320

DiSanti, M. A., Mumma, M. J., Russo, N. D., & Magee-Sauer, K. 2001, *Icarus*, 153, 361, doi: [10.1006/icar.2001.6695](https://doi.org/10.1006/icar.2001.6695)

DiSanti, M. A., Bonev, B. P., Gibb, E. L., et al. 2016, *ApJ*, 820, 34, doi: [10.3847/0004-637X/820/1/34](https://doi.org/10.3847/0004-637X/820/1/34)

Drozdovskaya, M. N., Bockelée-Morvan, D., Crovisier, J., et al. 2023, *A&A*, 677, A157, doi: [10.1051/0004-6361/202346402](https://doi.org/10.1051/0004-6361/202346402)

Feaga, L. M., & Sunshine, J. M. 2025, *PSJ*, 6, 95, doi: [10.3847/PSJ/adc094](https://doi.org/10.3847/PSJ/adc094)

Feaga, L. M., A'Hearn, M. F., Farnham, T. L., et al. 2014, *AJ*, 147, 24, doi: [10.1088/0004-6256/147/1/24](https://doi.org/10.1088/0004-6256/147/1/24)

Fitzsimmons, A., Hainaut, O., Meech, K. J., et al. 2019, *ApJL*, 885, L9, doi: [10.3847/2041-8213/ab49fc](https://doi.org/10.3847/2041-8213/ab49fc)

for Guides in Metrology, J. C. 2008, JCGM 101: Evaluation of Measurement Data - Supplement 1 to the "Guide to the Expression of Uncertainty in Measurement" - Propagation of Distributions Using a Monte Carlo Method, Tech. rep., JCGM

Fougere, N., Combi, M. R., Rubin, M., & Tenishev, V. 2013, *Icarus*, 225, 688, doi: [10.1016/j.icarus.2013.04.031](https://doi.org/10.1016/j.icarus.2013.04.031)

Harrington Pinto, O., Womack, M., Fernandez, Y., & Bauer, J. 2022, *PSJ*, 3, 247, doi: [10.3847/PSJ/ac960d](https://doi.org/10.3847/PSJ/ac960d)

Harris, C. R., Millman, K. J., van der Walt, S. J., et al. 2020, *Nature*, 585, 357, doi: [10.1038/s41586-020-2649-2](https://doi.org/10.1038/s41586-020-2649-2)

Hartogh, P., Crovisier, J., de Val-Borro, M., et al. 2010, *A&A*, 518, L150, doi: [10.1051/0004-6361/201014665](https://doi.org/10.1051/0004-6361/201014665)

Haser, L. 1957, *Bulletin de la Societe Royale des Sciences de Liege*, 43, 740

Haser, L., Oset, S., & Bodewits, D. 2020, *PSJ*, 1, 83, doi: [10.3847/PSJ/abc17b](https://doi.org/10.3847/PSJ/abc17b)

Haslam, C. G. T., Wilson, W. E., Graham, D. A., & Hunt, G. C. 1974, *A&AS*, 13, 359

Hopkins, M. J., Dorsey, R. C., Forbes, J. C., et al. 2025, *ApJL*, 990, L30, doi: [10.3847/2041-8213/adfbf4](https://doi.org/10.3847/2041-8213/adfbf4)

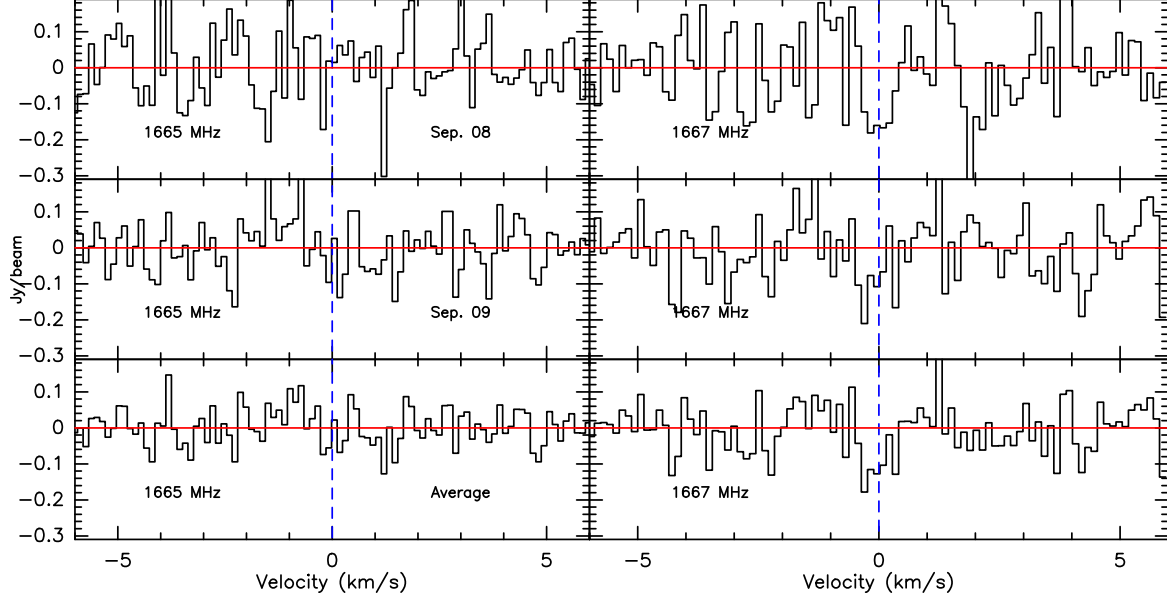


Figure C2. Averaged 18 cm OH lines of 3I/ATLAS observed on two separate days: September 8 (top), September 9 (middle), 2025, and weighted averages of the 1667 and 1665 MHz lines (bottom).

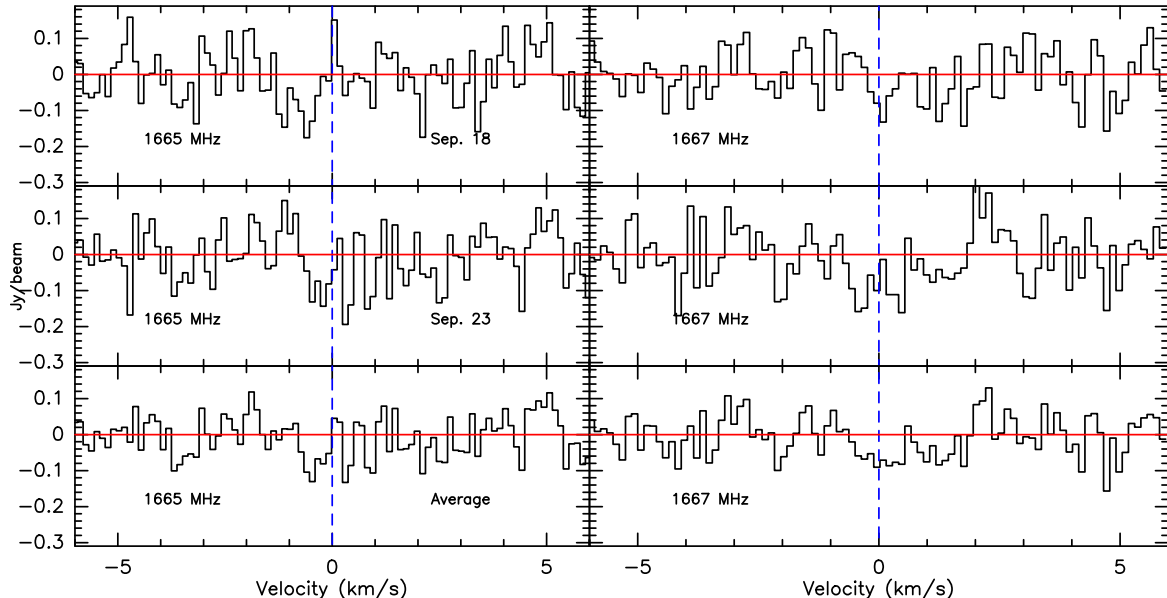


Figure C3. Averaged 18 cm OH lines of 3I/ATLAS observed on two separate days: September 18 (top), September 23 (middle), 2025, and weighted averages of the 1667 and 1665 MHz lines (bottom).

Hunter, J. D. 2007, Computing in Science and Engineering, 9, 90, doi: [10.1109/MCSE.2007.55](https://doi.org/10.1109/MCSE.2007.55)

Hutsemékers, D., Manfroid, J., Jehin, E., et al. 2025, arXiv e-prints, arXiv:2509.26053, doi: [10.48550/arXiv.2509.26053](https://doi.org/10.48550/arXiv.2509.26053)

Jewitt, D., Hui, M.-T., Mutchler, M., Kim, Y., & Agarwal, J. 2025, ApJL, 990, L2, doi: [10.3847/2041-8213/adf8d8](https://doi.org/10.3847/2041-8213/adf8d8)

Jewitt, D., & Luu, J. 2019, ApJL, 886, L29, doi: [10.3847/2041-8213/ab530b](https://doi.org/10.3847/2041-8213/ab530b)

Kareta, T., Noonan, J. W., Harris, W. M., & Springmann, A. 2023, PSJ, 4, 85, doi: [10.3847/PSJ/accc28](https://doi.org/10.3847/PSJ/accc28)

Kareta, T., Champagne, C., McClure, L., et al. 2025, ApJL, 990, L65, doi: [10.3847/2041-8213/adfbdf](https://doi.org/10.3847/2041-8213/adfbdf)

Knight, M. M., Schleicher, D. G., & Farnham, T. L. 2021, PSJ, 2, 104, doi: [10.3847/PSJ/abef6c](https://doi.org/10.3847/PSJ/abef6c)

Li, J., Shi, J., Ma, Y., & Sun, J. 2025a, AJ, 169, 126, doi: [10.3847/1538-3881/ada7e7](https://doi.org/10.3847/1538-3881/ada7e7)

Li, J., Shi, X., Shi, J., et al. 2025b, A&A, 701, A204, doi: [10.1051/0004-6361/202554867](https://doi.org/10.1051/0004-6361/202554867)

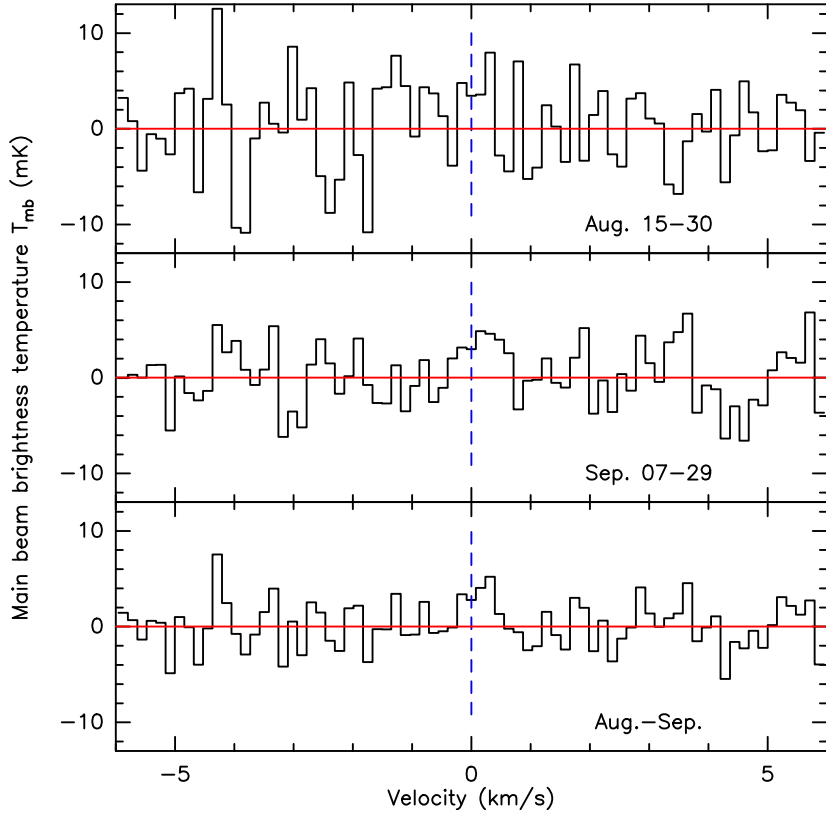


Figure C4. Averaged spectra of CO($J=1-0$) in 3I/ATLAS observed in August (top), September (middle), and from August to September (bottom). The red line is the base line. The vertical scale is the main beam brightness temperature and the horizontal scale is the Doppler velocity in the comet rest frame. The velocity resolution is $0.1587 \text{ km} \cdot \text{s}^{-1}$ after smooth.

Lisse, C. M., Bach, Y. P., Bryan, S., et al. 2025a, Research Notes of the American Astronomical Society, 9, 242, doi: [10.3847/2515-5172/ae0293](https://doi.org/10.3847/2515-5172/ae0293)

Lisse, C. M., Bach, Y. P., Bryan, S. A., et al. 2025b, arXiv e-prints, arXiv:2512.07318. <https://arxiv.org/abs/2512.07318>

Manfroid, J., Hutsemékers, D., & Jehin, E. 2021, Nature, 593, 372, doi: [10.1038/s41586-021-03435-0](https://doi.org/10.1038/s41586-021-03435-0)

McKay, A. J., DiSanti, M. A., Kelley, M. S. P., et al. 2019, AJ, 158, 128, doi: [10.3847/1538-3881/ab32e4](https://doi.org/10.3847/1538-3881/ab32e4)

Meech, K. J., Weryk, R., Micheli, M., et al. 2017, Nature, 552, 378, doi: [10.1038/nature25020](https://doi.org/10.1038/nature25020)

Opitom, C., Jehin, E., Hutsemékers, D., et al. 2021, A&A, 650, L19, doi: [10.1051/0004-6361/202141245](https://doi.org/10.1051/0004-6361/202141245)

Opitom, C., Snodgrass, C., Jehin, E., et al. 2025, MNRAS, 544, L31, doi: [10.1093/mnrasl/sla095](https://doi.org/10.1093/mnrasl/sla095)

Paganini, L., Mumma, M. J., Villanueva, G. L., et al. 2014, ApJ, 791, 122, doi: [10.1088/0004-637X/791/2/122](https://doi.org/10.1088/0004-637X/791/2/122)

Pety, J. 2018, in Submillimetre Single-dish Data Reduction and Array Combination Techniques, 11, doi: [10.5281/zenodo.1205423](https://doi.org/10.5281/zenodo.1205423)

Pisano, D. J., Smirnov, O. M., Ivchenko, M., Roth, L., & Buchner, S. 2025a, The Astronomer's Telegram, 17473, 1

Pisano, D. J., Smirnov, O. M., Ivchenko, M., et al. 2025b, The Astronomer's Telegram, 17499, 1

Protopapa, S., Kelley, M. S. P., Woodward, C. E., & Yang, B. 2021, PSJ, 2, 176, doi: [10.3847/PSJ/ac135a](https://doi.org/10.3847/PSJ/ac135a)

Protopapa, S., Kelley, M. S. P., Yang, B., et al. 2018, ApJL, 862, L16, doi: [10.3847/2041-8213/aad33b](https://doi.org/10.3847/2041-8213/aad33b)

Protopapa, S., Sunshine, J. M., Feaga, L. M., et al. 2014, Icarus, 238, 191, doi: [10.1016/j.icarus.2014.04.008](https://doi.org/10.1016/j.icarus.2014.04.008)

Remazeilles, M., Dickinson, C., Banday, A. J., Bigot-Sazy, M. A., & Ghosh, T. 2015, MNRAS, 451, 4311, doi: [10.1093/mnras/stv1274](https://doi.org/10.1093/mnras/stv1274)

Roth, N. X., Milam, S. N., Cordiner, M. A., et al. 2021, PSJ, 2, 55, doi: [10.3847/PSJ/abdd3a](https://doi.org/10.3847/PSJ/abdd3a)

Roth, N. X., Cordiner, M. A., Bockelée-Morvan, D., et al. 2025a, arXiv e-prints, arXiv:2511.20845, doi: [10.48550/arXiv.2511.20845](https://doi.org/10.48550/arXiv.2511.20845)

Roth, N. X., Milam, S. N., Cordiner, M. A., et al. 2025b, arXiv e-prints, arXiv:2511.05662, doi: [10.48550/arXiv.2511.05662](https://doi.org/10.48550/arXiv.2511.05662)

Rybicki, G. B. 1984, in Methods in Radiative Transfer, ed. W. Kalkofen, 21–64

Schleicher, D. G., & A'Hearn, M. F. 1988, ApJ, 331, 1058, doi: [10.1086/166622](https://doi.org/10.1086/166622)

Table D2. Pre-perihelion H₂O and CO production rate of 3I/ALTAS

Date (2025)	$\langle r_h \rangle$ [au]	$Q_{\text{H}_2\text{O}}$ [10^{27} s^{-1}]	Q_{CO} [10^{27} s^{-1}]	Instrument	Reference
Jul. 04	4.37	< 0.90	—	VLT	A. Alvarez-Candal et al. (2025)
Jul. 31-Aug. 01	3.50	0.74 ± 0.50	—	Swift	Z. Xing et al. (2025)
Aug. 06	3.31	0.22 ± 0.01	0.37 ± 0.02	JWST	M. A. Cordiner et al. (2025a)
Aug. 01-15	3.25	0.32 ± 0.06	0.1 ± 0.03	SPHEREx	C. M. Lisse et al. (2025b)
Aug. 18-20	2.90	1.36 ± 0.05	—	Swift	Z. Xing et al. (2025)
Aug. 28	2.64	0.25 ± 0.02	—	VLT	D. Hutsemékers et al. (2025)
Aug. 26-Spt. 03	2.54	< 9.46	—	TMRT	This work
Sep. 03-04	2.44	0.43 ± 0.02	—	VLT	D. Hutsemékers et al. (2025)
Sep. 07-29	2.01	—	5.75 ± 1.91	13.7m	This work
Sep. 08-09	2.27	14.52 ± 5.17	—	TMRT	This work
Sep. 10	2.25	1.23 ± 0.37	—	VLT	D. Hutsemékers et al. (2025)
Sep. 12	2.19	1.55 ± 0.36	—	VLT	D. Hutsemékers et al. (2025)
Sep. 18-23	1.96	20.79 ± 4.07	—	TMRT	This work
Oct. 13-16	1.43	57 ± 6	—	NRT	J. Crovisier et al. (2025)

Schloerb, F. P., & Gerard, E. 1985, AJ, 90, 1117, doi: [10.1086/113819](https://doi.org/10.1086/113819)

Seligman, D. Z., Micheli, M., Farnocchia, D., et al. 2025, ApJL, 989, L36, doi: [10.3847/2041-8213/adf49a](https://doi.org/10.3847/2041-8213/adf49a)

Shou, Y., Combi, M., Feaga, L., et al. 2025, Icarus, 435, 116557, doi: [10.1016/j.icarus.2025.116557](https://doi.org/10.1016/j.icarus.2025.116557)

Tan, H., Yan, X., & Li, J.-Y. 2026, arXiv e-prints, arXiv:2601.15443, doi: [10.48550/arXiv.2601.15443](https://doi.org/10.48550/arXiv.2601.15443)

Trigo-Rodríguez, J. M., Gritsevich, M., & Blum, J. 2025, arXiv e-prints, arXiv:2511.19112, doi: [10.48550/arXiv.2511.19112](https://doi.org/10.48550/arXiv.2511.19112)

Villanueva, G. L., Liuzzi, G., Faggi, S., et al. 2022, Fundamentals of the Planetary Spectrum Generator

Villanueva, G. L., Mumma, M. J., DiSanti, M. A., et al. 2011, Icarus, 216, 227, doi: [10.1016/j.icarus.2011.08.024](https://doi.org/10.1016/j.icarus.2011.08.024)

Wang, Z., Zhang, S.-B., Tseng, W.-L., et al. 2020, AJ, 159, 240, doi: [10.3847/1538-3881/ab8734](https://doi.org/10.3847/1538-3881/ab8734)

Woodward, C. E., Bockélee-Morvan, D., Harker, D. E., et al. 2025, PSJ, 6, 139, doi: [10.3847/PSJ/add1d5](https://doi.org/10.3847/PSJ/add1d5)

Xie, X., & Mumma, M. J. 1996, ApJ, 464, 457, doi: [10.1086/177336](https://doi.org/10.1086/177336)

Xing, Z., Bodewits, D., Noonan, J., & Bannister, M. T. 2020, ApJL, 893, L48, doi: [10.3847/2041-8213/ab86be](https://doi.org/10.3847/2041-8213/ab86be)

Xing, Z., Oset, S., Noonan, J., & Bodewits, D. 2025, ApJL, 991, L50, doi: [10.3847/2041-8213/ae08ab](https://doi.org/10.3847/2041-8213/ae08ab)

Yang, B., Meech, K. J., Connelley, M., Zhao, R., & Keane, J. V. 2025, ApJL, 992, L9, doi: [10.3847/2041-8213/ae08a7](https://doi.org/10.3847/2041-8213/ae08a7)

Yang, B., Li, A., Cordiner, M. A., et al. 2021, Nature Astronomy, 5, 586, doi: [10.1038/s41550-021-01336-w](https://doi.org/10.1038/s41550-021-01336-w)

Zakharov, V., Bockelée-Morvan, D., Biver, N., Crovisier, J., & Lecacheux, A. 2007, A&A, 473, 303, doi: [10.1051/0004-6361:20066715](https://doi.org/10.1051/0004-6361:20066715)

Zhang, Q., & Battams, K. 2025, arXiv e-prints, arXiv:2510.25035, doi: [10.48550/arXiv.2510.25035](https://doi.org/10.48550/arXiv.2510.25035)